

Check for updates

Electrochemical Self-Assembly of Boron-Based Cathode-Electrolyte Interphase to Stabilize 4.65 V LiCoO₂

Hengyu Ren, Xiaohu Wang, Wangyang Ding, Chunyu Xu, Wenguang Zhao, Haocheng Ji, Haocong Yi, Zhaohuang Zhan, Yongli Song, Lin Zhou, Qinghe Zhao,* and Feng Pan*

The cathode-electrolyte interphase (CEI) is vital for the stability of LiCoO₂ (LCO) beyond 4.55 V (vs Li/Li+). Herein, the full coverage of boron-based CEI is achieved on LCO surface via utilizing the self-wetting synthesis of boric acid (i.e., B-LCO), accompanying with the subsequent electrochemical self-assembly process upon cycles. Initially, the B-LCO is coated with borate deposits (size of 10-20 nm), then it melts and fully covers the surface upon sintering, leading to the full coverage of boron-based artificial CEI, which directly reduces the side reactions induced by highly oxidative Co^{4+}/O^{n-} (0 < n < 2). Significantly, during cycling, the in situ interfacial reactions between the surface boron-based species and LiF promote the formation of crystalline LiB₆O₀F components, showing the mechanically robust and highly Li⁺ conductive characteristics. Due to the synergism of robust CEI and structurally tough surface rocksalt (RS) phase, not only the more reversible phase transition and uniform Li+ (de)lithiation are achieved, but also the particle cracks and surface deterioration issues are effectively inhibited. As a result, the B-LCO||Li cells show excellent cycle stability, with a high retention of 84.0% in 500 cycles in 3-4.65 V.

H. Ren, X. Wang, W. Ding, C. Xu, W. Zhao, H. Yi, Z. Zhan, L. Zhou, O. Zhao, F. Pan

School of Advanced Materials

Peking University Shenzhen Graduate School

Peking University

Shenzhen 518055, China

E-mail: katong880109@163.com; panfeng@pkusz.edu.cn

W. Ding

School of Chemical and Biomolecular Engineering

The University of Sydney

Sydney, New South Wales 2008, Australia

H. Ji

 $Tsinghua-Berkeley\,Shenzhen\,Institute\,\&\,Tsinghua\,Shenzhen\,International\,Graduate\,School$

Tsinghua University

Shenzhen 518055, China

Y. Song

School of Energy and Power Engineering

Jiangsu University

Zhenjiang 212013, China



The ORCID identification number(s) for the author(s) of this article can be found under https://doi.org/10.1002/adfm.202504165

DOI: 10.1002/adfm.202504165

1. Introduction

LiCoO2 (LCO) has long been an irreplaceable cathode for Li-ion batteries in applications of 3C electronic products.[1] Recently, the research of advanced LCO has become the most concerned research hot spot in both the industry and academia, facing the rigorous requirements of batteries, such as the long cycle life, low temperature discharging ability, thermal stability, and high-rate charging/discharging abilities, etc.^[2] As the operating voltage rises beyond 4.55 V (vs Li/Li⁺), LCO undergoes hazardous O3/H1-3 phase transition, causing an increase in internal stress and inducing bulk cracks.[3] Meanwhile, the lattice oxygen participates in the redox reactions, leading to the oxidation and migration of bulk lattice O^{n-} (0 < n < 2), curved CoO_6 slabs, and the phase transition from layered to non-layered phases, such as the spinel, rocksalt (RS), etc., thus reducing the Li+ storage sites.[4] Comparing the bulk degradation, the surface deterioration is more severe, accompanying with severe Co/O

loss, intensive side reactions, etc., which greatly hinder the Li⁺ transport kinetics.^[5]

For surface optimization of LCO, achieving a complete, uniform, and thin coating is significant for the surface protection of LCO, which can also be regarded as the artificial cathodeelectrolyte interphase (CEI) on the materials before cycle operations. Such an ideal surface coating highlights the following characteristics. 1st, it emphasizes the coating completeness, which fundamentally isolates the contact between the surface oxidative Co^{4+}/O^{n-} (0 < n < 2) and electrolyte; 2nd, it highlights the coating uniformity, which ensures the uniform Li⁺ (de)lithiation process, and benefits for reducing the internal stress; 3rd, the thickness of coating must be limited to reduce the interface impedance for Li⁺ (de)lithiation. The present coating methods mainly include the sol-gel, solution reaction, dry ball milling, chemical vapor deposition (CVD), hydrothermal, and atomic layer deposition (ALD) methods, etc. [6] Among these coating methods, most of them are difficult to form an ideal coating on LCO surface, or require high cost, or stay far from industrial application. Therefore, developing low-cost and highly uniform coating synthesis is of great importance for the development of advanced LCO cathodes.

1616292. 2025, 41, Downloaded from https://ddvanced.onlinelibtrary.viely.com/doi/10.1002/admf.202504165 by University Town Of Shenzhen, Wiley Online Library on [1711/1025]. See the Terms and Conditions (https://onlinelibrary.wiley.com/terms-and-conditions) on Wiley Online Library or rules of use; OA articles are governed by the applicable Creative Commons License

www.afm-journal.de

Boron-based modification strategies have been widely reported before, which demonstrate excellent optimization effects on high-voltage cathode materials. From the doping aspect, the introduction of boron can effectively stabilize the lattice oxygen of materials (covalent B—O bonds), impact the micro-structures, and enhance overall structural stability.[7] From the coating aspect, amorphous boron oxide and lithium borate are commonly used as coating layers of cathode materials, which exhibit both protective properties and favorable Li⁺ transport kinetics and also demonstrate the feasibility of achieving low-cost and uniform "artificial CEI".[8] Meanwhile, the recent works of our group reveal that the in situ electrochemical reconstruction of CEI layer on LCO upon cycles can further strengthen interfacial stability and conductivity. [9] These findings highlight the critical importance of fundamental studies on the dynamic construction and evolution mechanisms of "artificial CEI" for enabling stable highvoltage LCO.[10]

Herein, we achieve the full coverage of boron-based coating by utilizing the self-wetting synthesis of boric acid (H₂BO₃) and systematically analyze its electrochemical reconstruction process. Initially, the B-LCO is coated with borate deposits (size of 10-20 nm), then it melts and fully covers on surface upon sintering, resulting in the full coverage of boron-based artificial CEI (3 nm) and surface RS phase (3 nm). The boron-based coating is composed with amorphous B2O3 and lithium borate, and shows uniform characteristics, acting as an "ideal" artificial CEI. Combined with surface RS phase, the surface modification completely isolates the contact between B-LCO and electrolyte and reduces the side reactions caused by highly oxidative Co^{4+}/O^{n-} (0 < n < 2). Notably, the in situ interfacial reaction between the boron-based species and LiF can promote the electrochemical self-assembly process upon cycles, and lead to the formation of a mechanically robust and highly Li+ conductive CEI, enriching with the crystalline LiB₆O₉F component, etc. Based on the above optimization, B-LCO achieves more reversible O3/H1-3 phase transition, and the particle cracks and surface deterioration are effectively inhibited. As a result, both the cycle and rate performances of B-LCO are greatly boosted. This work highlights the critical role of "ideal" surface coating on realizing robust CEI to reinforce the cell performances of LCO cathodes.

2. Results and Discussion

2.1. Full-Coverage of Artificial CEI on LCO Surface

For current coating strategies, no matter the solid coatings or the solution coatings, the full coverage of surface coating on the LCO surface is difficult to realize. Thus, the complete isolation between the highly oxidized $\text{Co}^{4+}/\text{O}^{n-}$ ions and electrolyte can hardly be realized upon charging. To solve this issue, here, we coat the surface of pristine LCO (P-LCO) with certain amount of borate deposits via solution treatment, which shows a nanoparticle size of ≈ 12 nm, and is uniformly distributed on P-LCO surface, as observed by high-resolution transmission electron microscope (HRTEM) (Figure S1, Supporting Information; Figure 1a). Then, these borate deposits progressively melt and fully cover the P-LCO surface upon sintering at a moderate temperature of 500 °C (Figure 1b,c). The detailed sintering process is shown in Figure S2 (Supporting Information) and the HRTEM images

of different particles with different scales are shown in Figures S3–S5 (Supporting Information). After sintering, a boron-based layer with thickness of 3 nm is obtained, which achieves a uniform and full coverage coating layer on the surface of B-LCO. The obtained surface coating presents amorphous characteristics, which benefit to reduce the degree of lattice anisotropy on P-LCO surface and help to homogenize the Li⁺ (de)lithiation kinetics upon cycle.

We further perform the X-ray diffraction (XRD) combined with Rietveld refinements to detect the phase structure of the P-LCO and B-LCO (Figure S6, Tables S1 and S2, Supporting Information). Both samples are well indexed to the typical layered α -NaFeO₂ structure with a space group of R-3 m, indicating that the surface boron modification has no influence on the bulk structure, and it only optimizes the surface chemistry. The existence of boron on surface of B-LCO, i.e., the characteristic peaks locating in the binding energy of 191.7 eV, is confirmed by Xray photoelectron spectroscopy (XPS) (Figure 1d), referring to the B-O bonds, and corresponding to the B₂O₃/LiBO₂/Li₃BO₃ components.[11] Meanwhile, for B-O peaks, the peak intensity decreases gradually as the etching depth increases, indicating the successful diffusion of B into the surface Co-O lattice with a depth of 30 nm. That is, the surface boron can not only form an amorphous surface layer but also enter into the surface Co-O lattice, inducing the Co-O structural reconstruction and regulating the stability of lattice oxygen.

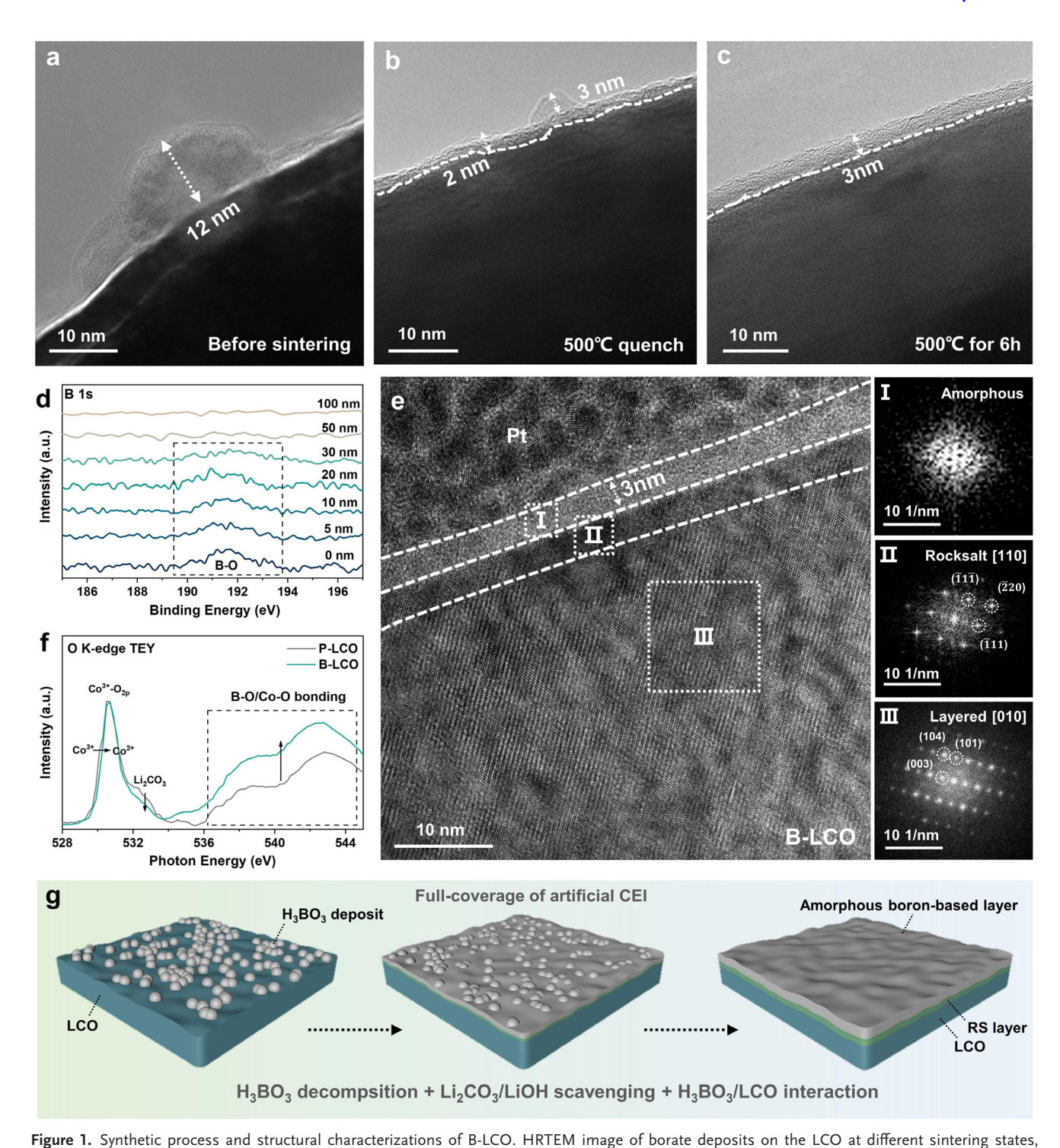
The cross-section images of P-LCO and B-LCO are also characterized by HRTEM with fast Fourier transform (FFT) after the milling process of focused ion beam (FIB) (Figure S7, Supporting Information; Figure 1e). P-LCO exists as the pure layered structure on the surface and bulk phase. For B-LCO, a thin amorphous phase layer with a thickness of 3 nm is observed, referring particularly to the boron-based amorphous layer. Energy dispersive spectrometer (EDS) line scanning and mapping results clearly show the enrichment of B element in the surface of B-LCO (Figure S8, Supporting Information). Meanwhile, adjacent to the surface amorphous layer, a RS phase with a thickness of 3 nm appears on B-LCO surface. The generation of surface RS phase is due to the interaction between layered LCO and boric acid coating process, leading to the "layered to RS" phase transition. As reported before, the polyanionic salt can promote to form some non-layer phases, including spinel and RS phases, etc.[12] And adjacent to the surface RS phase is the bulk layered phase.

We further perform the high-angle annular dark-field scanning transmission electron microscopy (HAADF-STEM) and electron energy loss spectroscopy (EELS) to characterize the ultra-thin surface structure. Figure \$9 (Supporting Information) clearly confirms the uniform and thin RS layer on the surface of B-LCO. For the EELS results (Figure S10, Supporting Information), the complete disappearance of Co L-edge peaks also shows the uniform distribution of surface amorphous layer, and the diminished O pre-peaks and the slight shift to lower energy loss for Co L-edge peaks confirm the surface RS layer. [13] The soft X-ray absorption spectroscopy (sXAS) of O K-edge spectra using total electron yield (TEY) mode is also applied to show the regulations of Co-O coordination chemistry by B element in a macroscopic perspective (Figure 1f). As observed, for B-LCO, the shift of the peak at 530.5 eV (the hybridization of Co³⁺ (e*_g)-O 2p) to higher photon energy shows the surface RS layer with some Co²⁺, which

16163028, 2025, 41, Downloaded

anced.onlinelibrary.wiley.com/doi/10.1002/adfm.202504165 by University Town Of Shenzhen, Wiley Online Library on [17/11/2025]. See the Terms and Conditions

inditions) on Wiley Online Library for rules of use; OA articles are governed by the applicable Creative Commons



a) before sintering (after solution treatment), b) just heat up to 500 °C and c) after sintering (500 °C for 6 h). d) The B 1s XPS patterns of B-LCO. e) HRTEM image and corresponding FFT results of B-LCO after FIB milling treatment. f) O K-edge spectra of TEY mode from sXAS measurements of P-LCO and B-LCO. g) The schematic diagram of full coverage of artificial CEI on B-LCO.

is consistent with the EELS results.^[14] The decreased peak locating at the photon energies of 533 eV in B-LCO refers to the removal of the Li_2CO_3 on the surface, which confirms that the H_3BO_3 can react with the surface residual lithium salts (such as LiOH, Li_2CO_3 etc.) and form some beneficial LiBO₂/Li₃BO₃

components.^[11c,15] Additionally, the higher peak intensities at photon energies of 535–545 eV indicate a splitting of the oxygen electronic orbitals, which is due to the synergistic effect between the boron-based artificial CEI and the RS phase, stabilizing the surface lattice oxygen.^[16]

16163028, 2025, 41, Downloaded from https://advanced.onlinelibrary.wiley.com/doi/10.1002/adfm.202504165 by University Town Of Shenzhen, Wiley Online Library on [17/11/2025]. See the Terms

ons) on Wiley Online Library for rules of use; OA articles are governed by the applicable Creative Commons

www.afm-journal.de

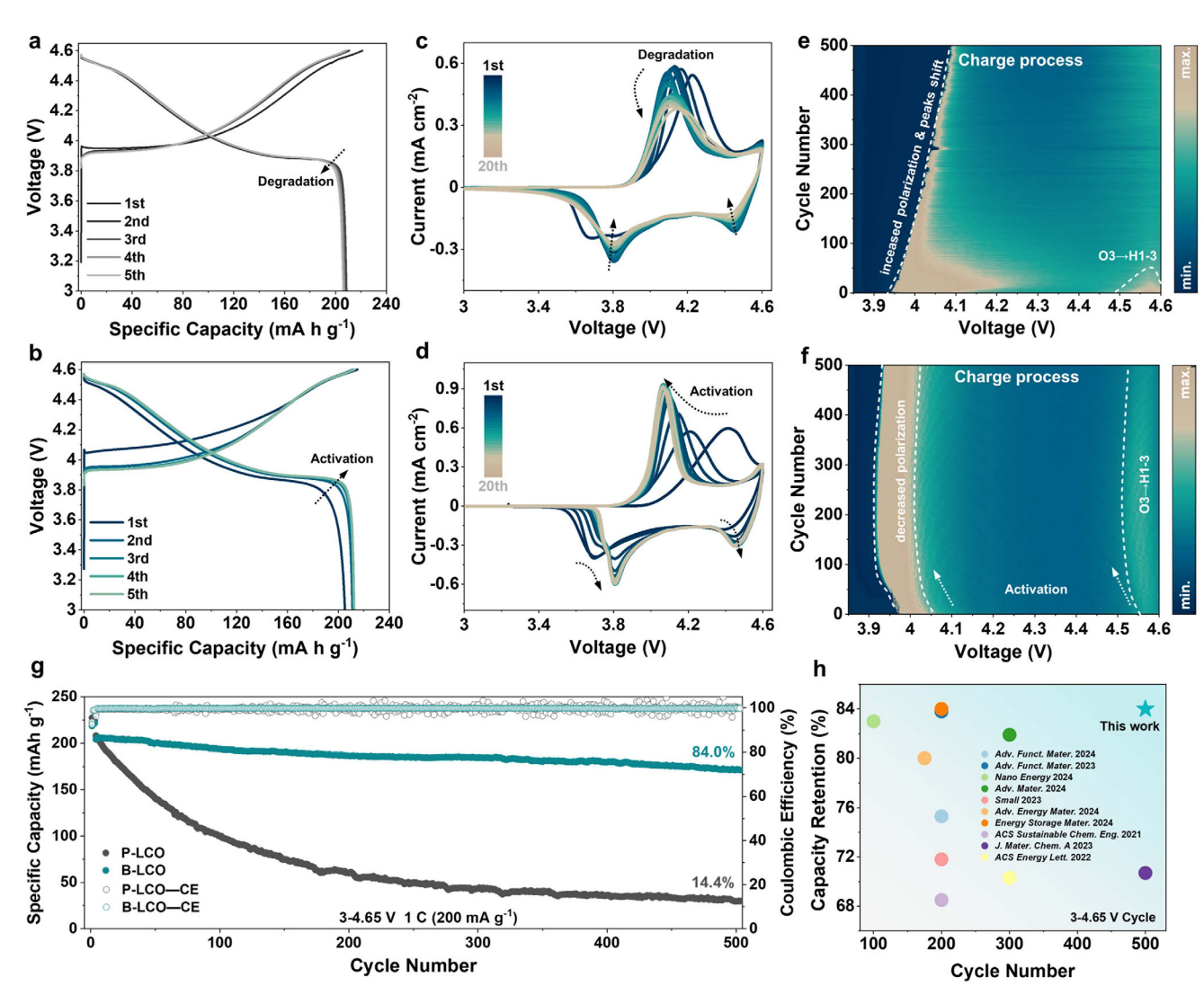


Figure 2. Capacity activation and cycle performance of B-LCO. Charge-discharge curves of a) P-LCO and b) B-LCO within a voltage range of 3–4.6 V at 0.2 C in the initial 5 cycles. CV tests of c) P-LCO and d) B-LCO within a voltage range of 3–4.6 V at a constant voltage scanning of 0.2 mV s⁻¹ for 20 cycles. The contour-map distributions of charge process of dQ/dV curves in 500 cycles for e) P-LCO and f) B-LCO. g) Cycle performance of P-LCO||Li cells within a voltage range of 3–4.65 V at 1 C. f) The electrochemical performance comparisons of the capacity retention within a voltage range of 3–4.65 V with the recently reported LCO.

Combining the above analyses, there forms a gradient surface structure of B-LCO, i.e., the gradient phase distribution from amorphous layer to RS, then to layered, with the gradient decrease of B doping in LCO surface. The schematic illustration for synthetic process of the gradient surface structure of B-LCO is shown in Figure 1g and Figure S11 (Supporting Information). The gradient surface structure is originated from the decomposition of H₃BO₃ and solid diffusion of boron ions into the surface lattice of B-LCO upon sintering, with a considerable diffusion depth of 30 nm. The boron-based amorphous layer completely covers the surface of B-LCO and acts as an artificial CEI, which primarily consists of B₂O₃, accompanied by a certain amount of LiBO₂/Li₃BO₃ and can effectively regulate the interface reactions upon cycles. The boron-containing surface RS phase has been regarded as effective stabilizer for the surface lattice oxygen and suppresses surface oxidative activity. Furthermore, surface-doped B ions are usually located in the tetrahedral positions in the intralayers of CoO_6 slabs, acting as the tough pillars to stabilize the layered structure. [7a,17]

2.2. Capacity Activation of B-LCO

As discussed above, a full-coverage artificial CEI with a thin RS layer is constructed on the surface of B-LCO. The evolution of this artificial CEI upon cycle is highly concerned, which plays a significant role on regulating the cell performances of B-LCO. Figure 2a,b shows the galvanostatic charge/discharge curves (at the current of 0.2 C) of the P-LCO||Li and B-LCO||Li cells in initial 5 cycles. For P-LCO, it shows a slow capacity decay, while for B-LCO, it shows a gradual capacity activation process, with the discharge capacity increasing gradually from 205.2 to 212.5 mA

ADVANCED
FUNCTIONAL
MATERIALS

16163028, 2025, 41, Downloaded from https://advanced.onlinelibrary.wiley.com/doi/10.1002/adfm.202504165 by University Town Of Shenzhen, Wiley Online Library on [17/11/2025]. See the Terms and Conditions (https://onlinelibrary.wiley.com/terms

and-conditions) on Wiley Online Library for rules of use; OA articles are governed by the applicable Creative Commons

h g $^{-1}$. The above difference is closely related to the regulated surface chemistry, as further identified by the cyclic voltammetry (CV) (with the scan rate of 0.2 mV s $^{-1}$, in 20 cycles) (Figure 2c,d). As observed, for P-LCO, the CV curves show two oxidation peaks and two reduction peaks, and the intensity of all redox peaks declines gradually in 20 cycles, indicating progressive surface deterioration. In contrast, for B-LCO, all the redox peaks exhibit a progressive activation characteristic, indicating that the surface of B-LCO is gradually activated upon cycles.

The activated surface chemistry of B-LCO can lead to the enhanced reversibility of bulk redox reactions upon cycle. Figure 2e,f shows the contour-map distributions of charge process of dQ/dV curves in 500 cycles (at the current of 1 C) (X-axis, the potential; Y-axis, the cycle number). There are two cathodic peaks located in 4.0 and 4.55 V, referring to the phase transitions of O3/O3' and O3'/H1-3, respectively. Compared with P-LCO, B-LCO presents more reversible cathodic peaks, with nearly no polarization increase and/or peak current decrease in 500 cycles, indicating the high reversibility of phase transitions. The discharge process exhibits the same changing trends (Figure S12, Supporting Information). In other words, the surface activation of B-LCO can benefit a lot on enhancing the bulk phase transition reversibility. As a result, both the cycle and rate performances of B-LCO are greatly enhanced. At 25 °C, the B-LCO||Li cell shows an impressive retention of 80.4% in 1000 cycles at the current of 1 C in the voltage range of 3–4.6 V (Figure S13a, Supporting Information), and a high retention of 84.0% in 500 cycles at the current of 1 C in 3-4.65 V (Figure 2g), which exhibits slight changes of charge/discharge average voltages upon cycles (Figure \$13b-d; Figure S14, Supporting Information). In Figure 2h and Table S4 (Supporting Information), we also list the cell performance comparison of different kinds of surface modifications of LCO, which show that B-LCO has a competitive performance upon high voltage operations (4.6 and 4.65 V). For B-LCO||graphite cell, it exhibits a high retention of 83.4% in 1000 cycles at the current of 1 C in 3–4.55 V (Figure S15, Supporting Information). Besides, attributing to the activated surface chemistry, the rate capacity of B-LCO||Li cell is also boosted, exhibiting a high capacity release of 139.1 mA h g⁻¹ at the current of 16 C in 3-4.6 V (Figure S16, Supporting Information). Therefore, both the cycle and rate performances of B-LCO are much superior than P-LCO, highlighting the beneficial role of activated surface chemistry of B-LCO.

2.3. Electrochemical Self-Assembly of Artificial CEI

The cell performance results clearly show the enhanced rate and cycle performances of B-LCO, relating closely to the electrochemical reconstruction of surface chemistry. To clarify this process, we perform the in situ electrochemical impedance spectroscopy (EIS) measurements of LCO||Li cells, and the obtained EIS plots are further analyzed by the distribution of relaxation time (DRT) technique, which provides a tough method to distinguish the dynamic characteristics based on the characteristic time constants (τ) . [18]

Figure S17 (Supporting Information) and Figure 3a–d compare the in situ EIS plots and the correlated DRT plots of LCO||Li and B-LCO||Li cells at the 2nd and 100th cycle, respectively. For DRT, the distribution of τ can be divided into three zones, i.e.,

zone I, in τ value range of 10^{-4} – 10^{-3} s, relating to the response to CEI ($R_{\rm CEI}$); zone II, in τ value range of 10^{-2} – 10^{-1} s, relating to the response to LCO surface structure without deterioration ($R_{\rm ct}$); and zone III, in τ value range of 10^{-1} – 10^{0} s, relating to the response to the greatly degraded LCO surface structure ($R_{\rm ct}$). Figure S17a,c (Supporting Information) and Figure 3a,b show the variation of $R_{\rm CEI}$ and $R_{\rm ct}$ of P-LCO cathodes in the 2nd and 100th charging/discharging process, respectively. In the 2nd cycle, there are significant changes in $R_{\rm ct}$ values, indicating that surface Co—O structure of P-LCO exhibits certain instability against the cyclic Li⁺ (de)lithiation. As observed, in the 100th cycle, the τ value of $R_{\rm ct}$ shifts toward the low-frequency region (zone III), which indicates the deterioration of surface Co—O structure.

Figure S17b,d (Supporting Information) and Figure 3c,d show the variation of $R_{\rm CEI}$ and $R_{\rm ct}$ of B-LCO cathode in the 2nd and 100th charging/discharging process, respectively. In the 2nd cycle, for B-LCO, both $R_{\rm CEI}$ and $R_{\rm ct}$ values are obviously higher than P-LCO, mainly attributing to the uniform surface optimization, including both the artificial CEI and surface RS phase. In the 100th cycle, both $R_{\rm CEI}$ and $R_{\rm ct}$ values increase greatly compared to the 2nd cycle, especially for the $R_{\rm CEI}$. For the τ value of $R_{\rm CEI}$, it shifts toward the lower frequency, i.e., mainly concentrates in the τ value of 10^{-3} s, showing the higher impedance and longer response time for the Li⁺/e⁻ transfer across the CEI and determining its superior protectiveness to surface structure of B-LCO, which demonstrate obvious evolution process. For the τ value of $R_{\rm ct}$ in 100th cycle, it is mainly located in zone II, indicating the well-preserved surface Co-O structure in 100 cycles.

The in situ differential electrochemical mass spectrometry (DEMS) and sXAS using TEY mode are applied to analyze the interface side reactions during the initial cycle. In Figure S18 (Supporting Information), there is almost no gas release for B-LCO||Li cell even charged to 4.65 V, while for P-LCO||Li cell, obvious gas release occurs during the charging process, including CO2, CO, and O₂, indicating the severe oxygen loss of P-LCO, which leads to the electrolyte solvents decomposition.^[19] Meanwhile, the O K-edge peaks of P-LCO also demonstrate the accumulation of Li₂CO₂ and organic decomposition product on the surface after 1 cycle (Figure \$19, Supporting Information). After the long-term cycles, the surface of cycled LCO cathodes are further characterized by HRTEM (Figure 3e,f). For P-LCO, its surface structure has transformed from pristine layered phase to the deteriorated RS phase, and the thickness of this RS phase is beyond 10 nm, which is the key structural factor for hindering the transfer of Li⁺/e⁻. The above "layered to RS" phase transition usually accompanies with the migration and release of highly oxidative lattice O^{n-} (0 < n < 2) upon cycle, resulting in the more severe side reactions, and preventing the formation of protective CEI. The diffraction pattern results further show some non-layered phase (i.e., spinel phase) appearing in the near-surface region of P-LCO, further confirming structure deterioration. By comparison, for B-LCO, the cycled surface still retains the same pristine RS phase with basically the same thickness of 5 nm, and the near-surface region still remains the layered phase. That is, the surface of B-LCO remains basically unchanged in 100 cycles at 4.6 V, thus the superior performance of B-LCO is mainly due to the protectiveness of robust CEI.

We conduct cryogenic transmission electron microscopy (cryo-TEM) with FFT to clarify the CEI evolution process.^[20] For

16163028, 2025, 41, Downloaded from https://advanced.onlinelibrary.wiley.com/doi/10.1002/adfm.202504165 by University Town Of Shenzhen, Wiley Online Library on [17/11/2025]. See the Terms

iditions) on Wiley Online Library for rules of use; OA articles are governed by the applicable Creative Commons

www.afm-journal.de

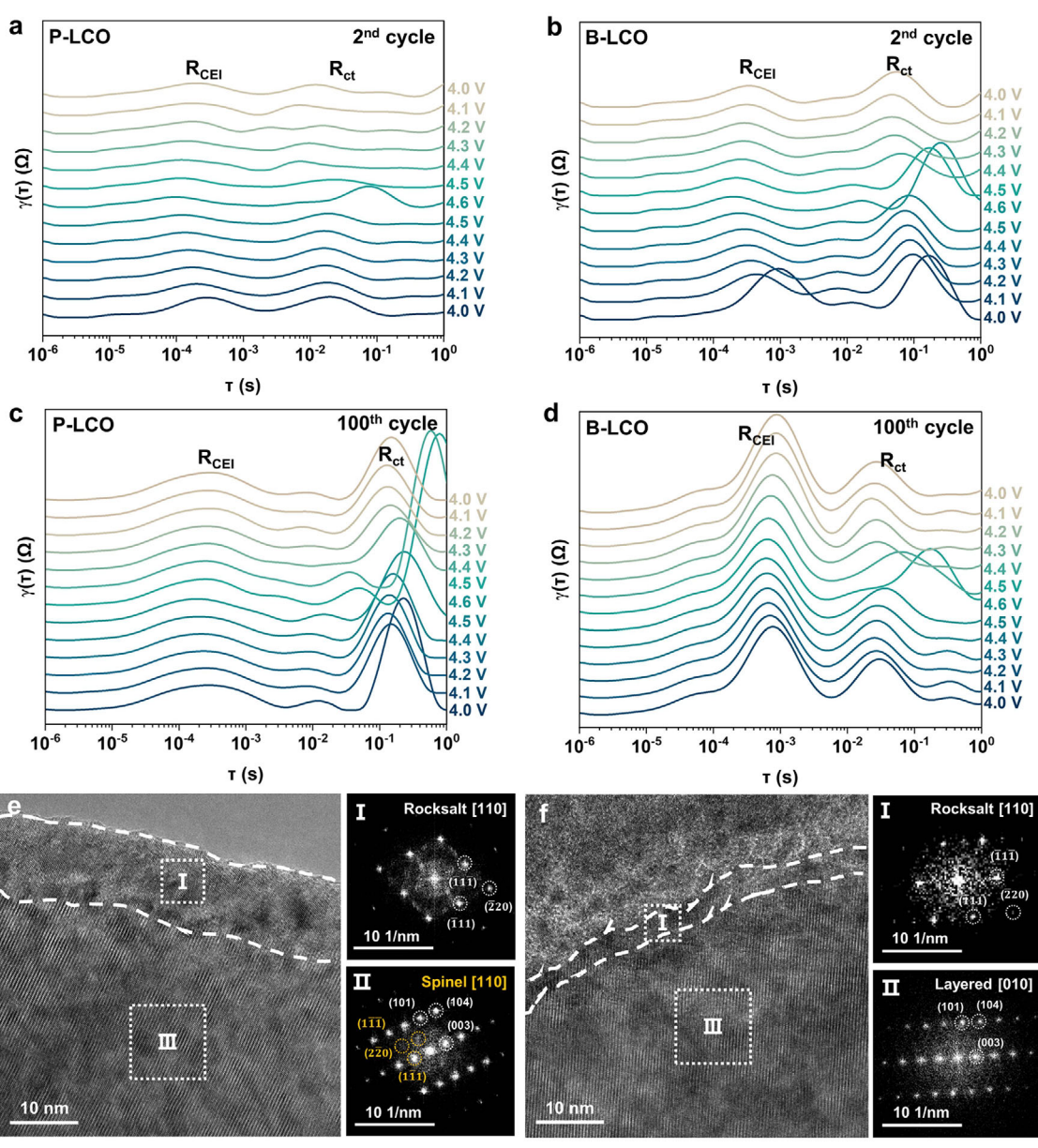


Figure 3. The differences of surface structure evolution for P-LCO and B-LCO upon cycles. The DRT curve based on the in situ EIS measurements of P-LCO||Li cells and B-LCO||Li cells at the a,b) 2nd, and c,d) 100th cycle within a voltage range of 3–4.6 V at 0.2 C. The HRTEM image and corresponding FFT results of e) P-LCO and f) B-LCO after 100 cycles.

P-LCO, the obtained CEI shows uneven and loose characteristics and is in an amorphous state, therefore presents a weak protectiveness, as shown in **Figure 4a**,b, Figures S20a,S21 (Supporting Information). While for B-LCO, the protectiveness of CEI mainly comes from the self-assembly properties, including the chemical composition, density, thickness, etc. Figure 4c,d, Figures S20b,S22 (Supporting Information) show the cryo-TEM characterization and diffraction pattern of the cycled CEI. The results show that the CEI of B-LCO exhibits uniform and compact characteristics with the thickness increasing from 2–5 to 10–15 nm, and it evolves from an amorphous state with B—O components to a certain amount of inorganic substances with ordered crystal structures, such as LiF, LiB₆O₉F, etc.

We further perform the cryo-TEM characterization on B-LCO after the 2nd, 30th, and 50th cycles to elucidate the detailed CEI evolution process. After 2 cycles (Figure S23a,b, Supporting Information), the thickness of CEI is 3–10 nm, where FFT analysis confirms the deposition of LiF nanoparticles derived from decomposition of LiPF $_6$ at the interface during the Li+ (de)lithiation. After 30 cycles (Figure S23c,d, Supporting Information), the CEI on B-LCO thickens to \approx 10 nm with further LiF accumulation. After 50 cycles (Figure S23e,f, Supporting Information), the CEI reaches 10–15 nm, and FFT patterns reveal characteristic diffraction rings corresponding to the (212) and (111) crystal planes of LiB $_6$ O $_9$ F, indicating the crystallization of amorphous boron-based coating. Complemented by the

16163028, 2025, 41, Downloaded

nelibrary.wiley.com/doi/10.1002/adfm.202504165 by University Town Of Shenzhen, Wiley Online Library on [17/11/2025]. See the Terms

onditions) on Wiley Online Library for rules of use; OA articles are governed by the applicable Creative Commons

www.afm-journal.de

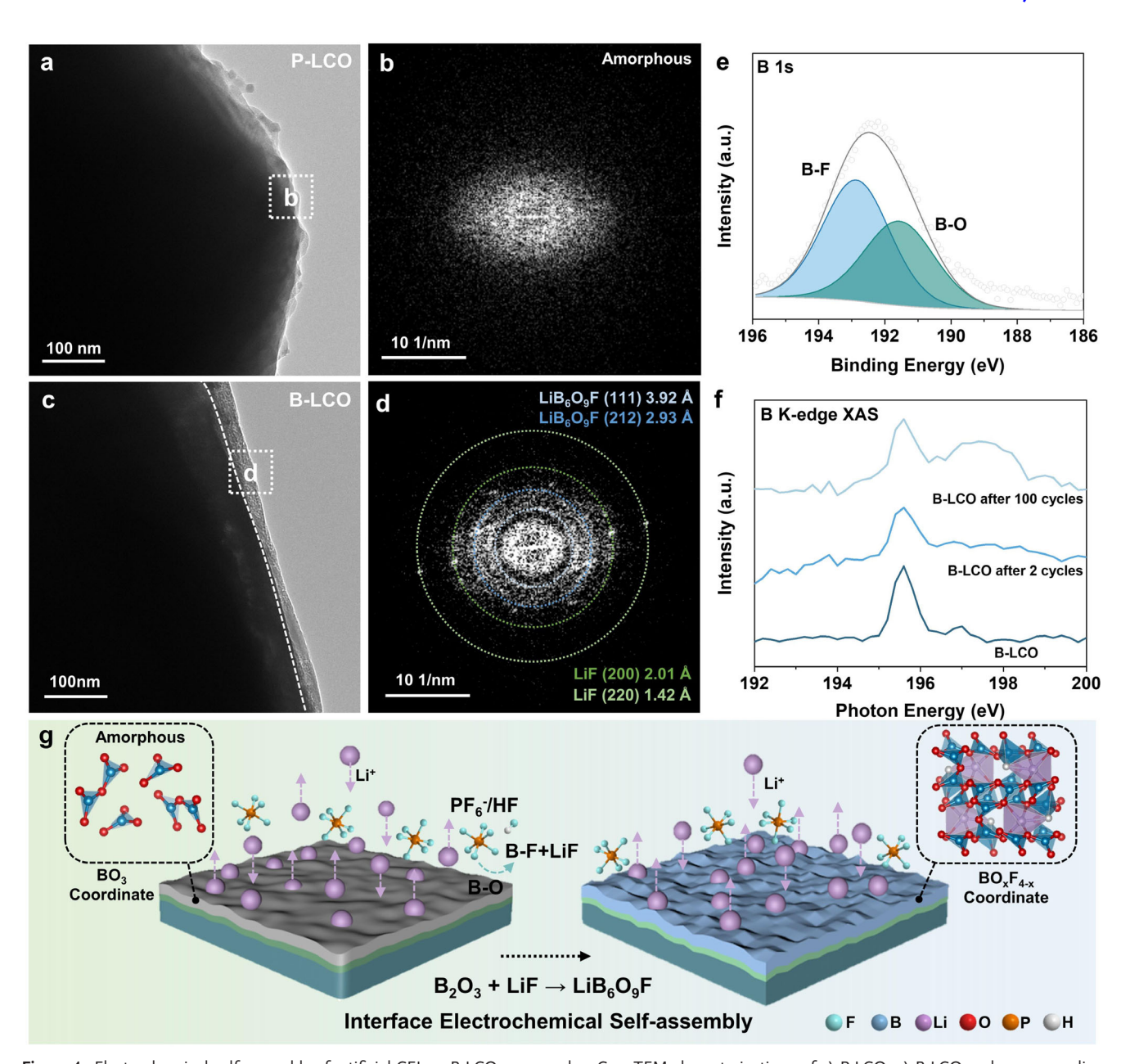


Figure 4. Electrochemical self-assembly of artificial CEI on B-LCO upon cycles. Cryo-TEM characterizations of a) P-LCO, c) B-LCO and corresponding c,d) FFT analysis after 100 cycles within a voltage range of 3–4.6 V at 1 C. e) The B 1s XPS patterns of B-LCO after 100 cycles. f) B K-edge spectra of TEY mode from sXAS measurements of pristine B-LCO, B-LCO after 2 cycles, and B-LCO after 100 cycles within a voltage range of 3–4.6 V at 1 C. g) The schematic diagram of the mechanism of electrochemical self-assembly of CEI on B-LCO.

above CEI images of B-LCO after 100 cycles, the CEI evolves into a denser, more uniform structure enriched with both LiB $_6$ O $_9$ F and LiF components. Thus, based on the cryo-TEM results, the initially formed boron-based CEI layer, which is predominantly composed of amorphous B $_2$ O $_3$ with a disordered configuration, undergoes an in situ electrochemical self-assembly process during cycling, gradually transforming to a crystalline CEI layer that incorporates the ordered LiB $_6$ O $_9$ F components.

Meanwhile, during the evolution of this artificial CEI, LiF deposits are distributed throughout the entire CEI layer, rather than being solely concentrated on the outer CEI region (electrolyte-

CEI side). This observation confirms that electrolyte components can penetrate into the inner CEI region (CEI-LCO side) across the amorphous CEI layer, and further highlights the importance of surface RS phase of B-LCO, which avoids the oxidation of electrolyte solvents.

The proposed evolution process can be further validated through spectroscopic and electrochemical characterization. B 1s XPS results (Figure 4e) also reveal that the self-assembly B-LCO CEI contains both the B—F and B—O bonds, located at binding energies of 193.0 and 191.7 eV, respectively. For C 1s and F 1s XPS results (Figure S24, Supporting Information), fewer organic

www.advancedsciencenews.com



www.afm-journal.de

1616292, 2025, 41, Downloaded from https://widennced.onlinelibrary.wiely.com/civ/10.1002/aft.202504165 University Town O'S benzhen, Wiley Online Library on [17/11/1025]. See the Terms and Conditions (https://onlinelibrary.wiely.com/terms-and-conditions) on Wiley Online Library or rules of use; OA articles are governed by the applicable Creative Commons License

solvents decomposition products (Figure S24a,b, Supporting Information) and more LiF species (Figure S24c,d, Supporting Information) are enriched in the CEI of B-LCO compared with CEI of P-LCO, indicating that the formation of LiF at the interface of B-LCO is not originated from the LiPF $_6$ hydrolysis which is facilitated by carbonate solvent decomposition, but proceeds through alternative reaction pathways. [21] Besides, sXAS of B K-edge spectra using TEY mode (Figure 4d) show that there exist new characteristic peaks appearing in the photon energy range of 196.5–200 eV, referring to the evolution from 3-coordinate B ion (BO $_3$ coordinates) to 4-coordinate B ion (BO $_x$ F $_{4-x}$ coordinates) in the self-assembled CEI. [22]

Introducing the inorganic LiF/LiB $_6O_9F$ species boosts the Li⁺ transport kinetics of B-LCO. We further characterize the average Li⁺ transport kinetics of B-LCO using galvanostatic intermittent titration technique (GITT). Figure \$25 (Supporting Information) shows the variations of the calculated Li⁺ diffusion coefficient ($D_{\text{Li+}}$) of LCO cathodes in the 2nd and 50th cycles, respectively. For P-LCO, the $D_{\text{Li+}}$ value in 50th cycle is much lower than that in the 2nd cycle, which is mainly due to the seriously deteriorated surface structure. While for B-LCO, the $D_{\text{Li+}}$ value in the 50th cycle is significantly reinforced than in the 2nd cycle, mainly due to the self-assembly CEI with the generation of highly conductive inorganic species, including LiF, LiB $_6O_9F$, etc.

Combining the above results, the mechanism of electrochemical self-assembly for CEI of B-LCO is revealed (Figure 4e): 1) The uniform, full-covered, and boron-based CEI on B-LCO effectively suppresses organic solvent decomposition and CO₂/H₂O evolution under high voltages. Meanwhile, a small amount of HF reacts with B-O bonds to generate B-F bonds and H2O. This process further drives LiPF₆ decomposition at the interface during Li⁺ (de)lithiation, generating substantial LiF species; 2) the in situ interfacial reaction of LiF and boron-based species during cycling, promoting the formation of LiB₆O₉F components. And, this low-temperature synthesis of LiB₆O₀F serves as the fundamental basis for the aforementioned interfacial reactions.^[23] These processes drive the structural evolution of the CEI, transforming from a disordered amorphous state to an ordered crystalline phase, while simultaneously promoting CEI densification and enhancing the Li⁺ transport kinetics of B-LCO.

2.4. More Uniform Li+ (de)Lithiation

In addition to the enhanced interface structure stability caused by CEI activation, for B-LCO, due to the formation of full-covered and compact CEI, the uniformity of Li⁺ (de)lithiation or the bulk phase transition is also greatly improved. The uniformity of Li⁺ (de)lithiation can be characterized by HRTEM and XRD, in which HRTEM can characterize the particle cracks and lattice distortions and slippages caused by the uneven Li⁺ (de)lithiation, and XRD shows the variation of layer spacing upon cycle, closely relating to the uniformity of Li⁺ (de)intercalation behaviors. Generally, for LCO, there are several reasons that can lead to uneven Li⁺ (de)lithiation, including the different orientations of exposed lattices of LCO surface, uneven surface coating, and uneven point contacts between LCO and conductive agents, etc. [6a.24] The uneven Li⁺ (de)lithiation will inevitably lead to the over-charging of partial CoO₆ slabs, causing deep phase transition and increased

internal stress, thus leading to formation of internal cracks. Once these cracks extend to the surface, more side reaction occurs, causing the deterioration of electrolyte chemistry upon cycle, and reducing the stability of LCO-based cells.

Figure S26 (Supporting Information) compares the in situ XRD patterns of LCO||Li cells in the 1st cycle. Comparing the variations of (003) peaks located at 2theta of 18.9 degrees, P-LCO exhibits a collective glide of CoO6 slabs, indicating the progressive O3/O3'/H1-3 phase transition upon charging, while for B-LCO, the pristine O3 phase retains until 1st charging to 4.05 V. The significant difference between two kinds of LCO cathodes is closely related to the uniform surface modification of B-LCO, which contributes to the ordered and more uniform Li+ (de)lithiation. As charging to 4.6 V, we further analyze the (003) peaks from the in situ XRD patterns. The (003) peaks at charged state can be divided into three peaks, including O3', O3'/H1-3 (the intergrowth of O3' and H1-3 phases) and H1-3 phases, locating at 2theta of 18.9, 19.2, and 19.6 degrees, respectively, in which, the O3'/H1-3 and H1-3 phases can be both considered as the hybrid of O1 and O3 phases, and H1-3 contains higher content of O1 phase than that of O3'/H1-3.[25] As observed, the total proportion of O3'/H1-3 and H1-3 phases of the charged B-LCO is obviously lower than P-LCO, indicating that the surface optimization can suppress the O3/H1-3 phase transition upon charging, benefiting the long-term structure stability of B-LCO. Meanwhile, the half-width of the characteristic peaks of O3 phase of B-LCO is obviously wider than P-LCO, indicating the uniformly distributed O3 phase in bulk LCO, further confirming the more uniform Li+ (de)lithiation.

Figure 5a,b compare the surface structures of charged LCO cathodes (at 4.6 V, 1st cycle). For the charged cathodes, both their near-surface regions exhibit the layered/spinel hybrid phases. That is, at charged state, the near surface of LCO inevitably undergoes certain Co/O migrations, thus leading to "layer/spinel" phase transition. The most significant difference in the nearsurface structure of LCO cathodes is that, for P-LCO, the diffraction pattern shows the interlink of diffraction spots, indicating the highly distorted and slipping CoO6 slabs, while for B-LCO, the diffraction spots are very clear, representing the relatively flat CoO₆ slabs or the well-maintained layered structure. The distortion and slippage of CoO₆ slabs of charged LCO have been regarded as one of the key indexes for determining the high voltage stability of LCO, which is closely related to the uniformity of Li⁺ (de)lithiation. The more uniform of the Li⁺ (de)lithiation, the lower degree of CoO₆ slabs' distortion and slippage of the charged LCO. In Figure S27 (Supporting Information), large-scale of HRTEM images in different regions can confirm the above phenomenon. Figure 5c-f compares the macroscopic scanning electron microscopy (SEM) and cross-section HRTEM images of LCO cathodes after 100 cycles. It is observed that, for P-LCO, huge cracks are generated in both the surface and bulk regions. While for B-LCO, due to the more uniform Li⁺ (de)lithiation, the particle integrity is well retained, with nearly no cracks forming in both surface and bulk regions. Figure \$28 (Supporting Information) compares the ex situ XRD patterns of the cycled LCO cathodes (at the 100th cycle). For P-LCO, it shows a significant left shift and an obvious increase in the half-width of (003) peak, indicating the increased disorder of layered structure. While for B-LCO, the (003) peak remains the same to its pristine state,

16163028, 2025, 41, Downloaded from https://advanced.onlinelibrary.wiley.com/doi/10.1002/adfm.202504165 by University Town Of Shenzhen, Wiley Online Library on [17/11/2025]. See the Terms and Conditions (https://onlinelibrary.wiley

onditions) on Wiley Online Library for rules of use; OA articles are governed by the applicable Creative Commons

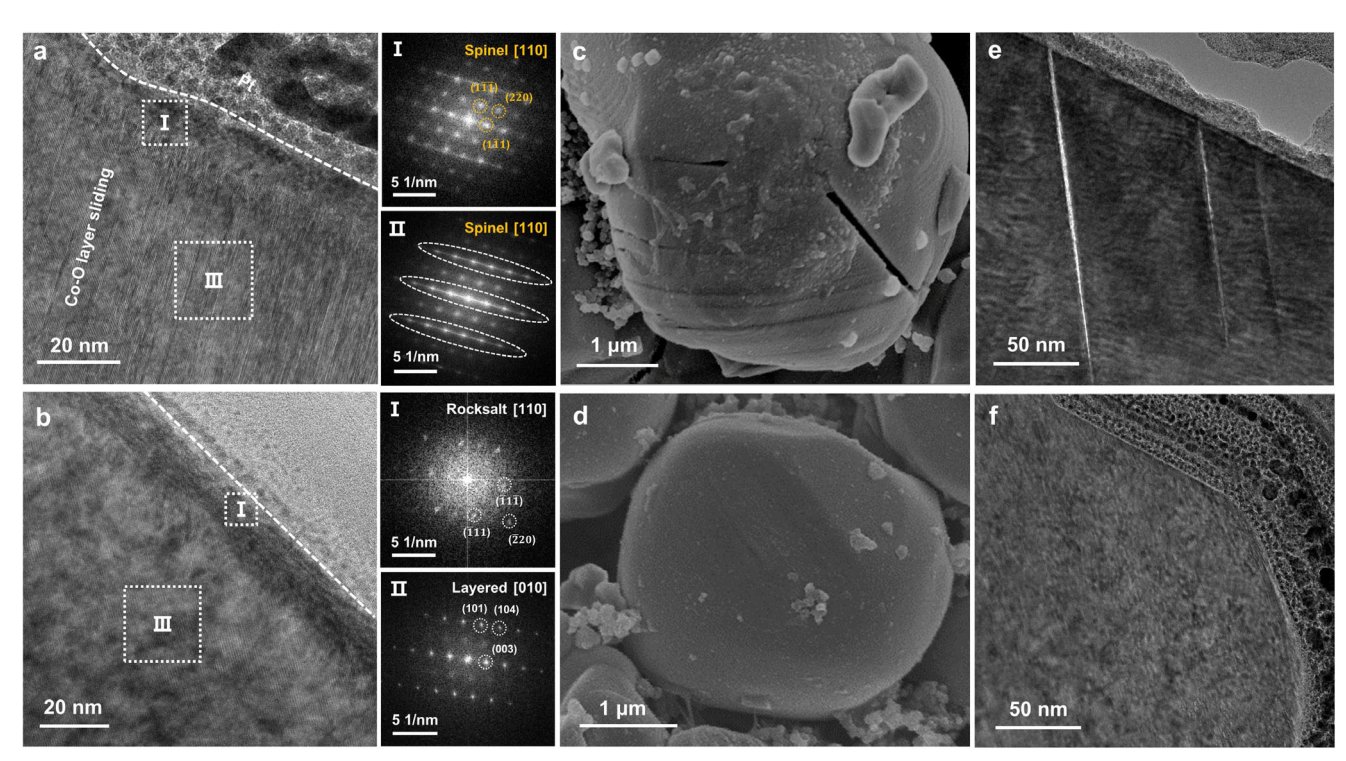


Figure 5. Uniformity of Li⁺ (de) lithiation and phase transition of B-LCO. The HRTEM image and corresponding FFT results of a) P-LCO and b) B-LCO at 4.6 V charged state in the 1st cycle within a voltage range of 3–4.6 V at 0.2 C. The SEM and HRTEM images of c,e) P-LCO and d,f) B-LCO after 100 cycles within a voltage range of 3–4.6 V at 1 C.

showing the high stability of layered structure due to the more uniform (de)lithiation.

After all, in this work, we highlight the full coverage of artificial CEI by utilizing the chemical self-wetting synthesis of borate species on B-LCO, the electrochemical self-assembly process of this CEI upon cycles, the well-protected surface structure, as well as the promoted uniformity of Li⁺ (de)lithiation. The optimization mechanism is illustrated in **Figure 6**. For P-LCO, the surface layered structure is relatively fragile. When charged to 4.6 V, the higher state of charge (SOC) and uneven delithiation of LCO cause severe distortion and slippage of CoO₆ slabs, Co/O migration, and more side reactions, etc. Upon long-term cycles, the surface is inevitably deteriorated, and the formation of protective CEI is hardly to be realized. Meanwhile, the uneven Li⁺ (de)lithiation also leads to particle cracking and deterioration of electrolyte chemistry. Thus, P-LCO shows the poor cycle stability.

For B-LCO, the surface can be well protected by the full coverage of artificial CEI, and a thin surface RS phase is constructed to enhance the mechanical strength of surface Co—O structure. This artificial CEI completely isolates the contact between the highly oxidative $\text{Co}^{4+}/\text{O}^{\text{n}}$ and the electrolyte, thus greatly reducing the side reactions. More importantly, the amorphous and boron-based CEI undergo the electrochemical self-assembly process upon cycle, accompanying with an increase in thickness, and the formation of crystalline $\text{LiB}_6\text{O}_9\text{F}$ species, thus providing enhanced protection on surface Co—O structure, and the promoted Li^+ transport kinetics across the CEI. Besides, this self-assembly CEI also enables the uniformity of Li^+ (de)lithiation and effectively suppresses the generation of particle cracks. Overall, due to

the presence of uniform CEI, not only the highly reversible phase transition is guaranteed but also the crack's formation and surface deterioration are inhibited, thus greatly enhancing the cycle stability of B-LCO when cycled beyond 4.6 V.

The obtained results above show a feasible synthesis of high-quality artificial CEI, the corresponding electrochemical reconstruction process, and its beneficial role in enhancing cycle stability of LCO. Currently, the demand for high-capacity cathodes is very urgent in industry, especially for layered transition metal oxide cathodes with high reversible capacity beyond 210 mA h g⁻¹. From the aspect of material research, the top priority is to address the surface issue, mainly via inhibiting the structure deterioration caused by Co/O loss, then, tackling the issue of bulk stability is also necessary, which is more complex considering the balance between high discharge capacity and inferior bulk stability. This work provides a possible route for solving the surface issue, and we hope that the industry can give more insight on exploring how to achieve low-cost and more uniform coating on layered transition metal oxide cathodes.

3. Conclusion

This work develops a low-cost synthesis to realize an "ideal" surface coating of LCO, via utilizing the self-wetting characteristics of borate salts. The amorphous boron-based layer is completely and uniformly coated on surface of B-LCO, with a thickness of 3 nm, and it can react with LCO surface to form a thin surface RS phase. The surface RS phase reinforces the mechanical strength of surface structure. Significantly, the full coverage of this

16163028, 2025, 41, Downloaded from https://advanced.onlinelibrary.wiley.com/doi/10.1002/adfm.202504165 by University Town Of Shenzhen, Wiley Online Library on [17/11/2025]. See the Terms

conditions) on Wiley Online Library for rules of use; OA articles are governed by the applicable Creative Commons

www.afm-journal.de

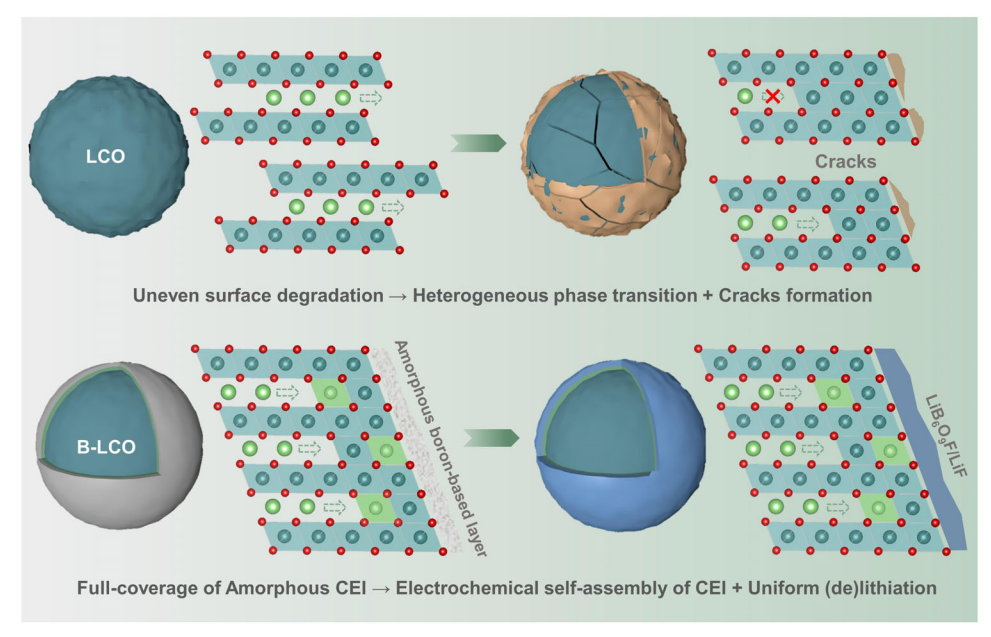


Figure 6. The schematic diagram of the full coverage of boron-based artificial CEI on B-LCO and its electrochemical self-assembly process upon cycles to stabilize the LCO at the voltage up to 4.6/4.65 V.

artificial CEI is not just acted as the physical barrier to completely isolate the contact between B-LCO surface and electrolyte, the electrochemical self-assembly process also promotes the formation of a more stable and robust CEI, enriching with inorganic LiF/LiB $_6$ O $_9$ F species, and with a thickness of 10–15 nm. As a result, the optimized CEI and thin RS layer enable a more uniform Li $^+$ (de)lithiation, thus reducing LCO particle cracking when cycled beyond 4.6 V. This work proposes a feasible synthesis to realize "ideal" surface coating of LCO and reveals its evolution process upon cycles, which will guide a lot on developing the more advanced LCO cathodes.

Supporting Information

Supporting Information is available from the Wiley Online Library or from the author.

Acknowledgements

H.R., X.W., and W.D. contributed equally to this work. This work was financially supported by the National Natural Science Foundation of China (No. 92472206), the Major Science and Technology Infrastructure Project of Material Genome Big-science Facilities Platform supported by Municipal Development and Reform Commission of Shenzhen, the International Joint Research Center for Electric Vehicle Power Battery and Materials (No. 2015B01015), Guangdong Key Laboratory of Design and Calculation of New Energy Materials (No. 2017B030301013), Shenzhen Key Laboratory of New Energy Resources Genome Preparation and Testing (No. ZDSYS201707281026184). This work also thank the staff members of MCD-A and MCD-B beamlines at National Synchrotron Radiation Laboratory (NSRL) in Hefei, for providing technical support and assistance in data collection and analysis.

Conflict of Interest

The authors declare no conflict of interest.

Data Availability Statement

The data that support the findings of this study are available from the corresponding author upon reasonable request.

Keywords

CEI, electrochemical self-assembly, ${\rm LiCoO_2}$, phase transition, uniform coating

Received: February 14, 2025 Revised: April 4, 2025 Published online: April 26, 2025

- [1] K. Mizushima, P. C. Jones, P. J. Wiseman, J. B. Goodenough, *Mater. Res. Bull.* 1980, 15, 783.
- [2] J.-J. Fang, Y.-H. Du, Z.-J. Li, W.-G. Fan, H.-Y. Ren, H.-C. Yi, Q.-H. Zhao, F. Pan, J. Electrochem. 2024, 30, 2314005.
- [3] a) H. Ren, W. Zhao, H. Yi, Z. Chen, H. Ji, Q. Jun, W. Ding, Z. Li, M. Shang, J. Fang, K. Li, M. Zhang, S. Li, Q. Zhao, F. Pan, Adv. Funct. Mater. 2023, 33, 2302622; b) X. Wang, H. Ren, Y. Du, Z. Li, W. Zhao, H. Ji, H. Yi, Q. Pan, J. Liu, Z. Lou, L. Zhou, F. Pan, Q. Zhao, Nano Energy 2024, 125, 109537.
- [4] a) J. Li, C. Lin, M. Weng, Y. Qiu, P. Chen, K. Yang, W. Huang, Y. Hong, J. Li, M. Zhang, C. Dong, W. Zhao, Z. Xu, X. Wang, K. Xu, J. Sun, F. Pan, Nat. Nanotechnol. 2021, 16, 599; b) C. Lin, J. Li, Z. W. Yin, W. Huang, Q. Zhao, Q. Weng, Q. Liu, J. Sun, G. Chen, F. Pan, Adv. Mater. 2023, 36, 2307404.
- [5] H. Ren, G. Zheng, Y. Li, S. Chen, X. Wang, M. Zhang, W. Zhao, H. Yi, W. Huang, J. Fang, T. Liu, L. Yang, M. Liu, Q. Zhao, F. Pan, Energy Environ. Sci. 2024, 17, 7944.
- [6] a) U. Nisar, N. Muralidharan, R. Essehli, R. Amin, I. Belharouak, Energy Storage Mater. 2021, 38, 309; b) Q. Liu, Y.-T. Liu, C. Zhao, Q.-S. Weng, J. Deng, I. Hwang, Y. Jiang, C. Sun, T. Li, W. Xu, K. Du, A. Daali, G.-L. Xu, K. Amine, G. Chen, ACS Nano 2022, 16, 14527.



www.advancedsciencenews.com



16163028, 2025, 41, Downloaded from https://advanced.onlinelibrary.wiley.com/doi/10.1002/adfm.202504165 by University Town Of Shenzhen, Wiley Online Library on [17/11/2025]. See the Terms and Conditions (https://advanced.onlinelibrary.wiley.com/doi/10.1002/adfm.202504165 by University Town Of Shenzhen, Wiley Online Library on [17/11/2025]. See the Terms and Conditions (https://advanced.onlinelibrary.wiley.com/doi/10.1002/adfm.202504165 by University Town Of Shenzhen, Wiley Online Library on [17/11/2025]. See the Terms and Conditions (https://advanced.onlinelibrary.wiley.com/doi/10.1002/adfm.202504165 by University Town Of Shenzhen, Wiley Online Library on [17/11/2025]. See the Terms and Conditions (https://advanced.onlinelibrary.wiley.com/doi/10.1002/adfm.202504165 by University Town Of Shenzhen, Wiley Online Library on [17/11/2025]. See the Terms and Conditions (https://advanced.onlinelibrary.wiley.com/doi/10.1002/adfm.202504165 by University Town Of Shenzhen, Wiley Online Library on [17/11/2025]. See the Terms and Conditions (https://advanced.onlinelibrary.wiley.com/doi/10.1002/adfm.202504165 by University Town Of Shenzhen, Wiley Online Library on [17/11/2025]. See the Terms and Conditions (https://advanced.onlinelibrary.wiley.com/doi/10.1002/adfm.202504165 by University Town Of Shenzhen, Wiley Online Library on [17/11/2025]. See the Terms and Conditions (https://advanced.onlinelibrary.wiley.com/doi/10.1002/adfm.202504165 by University Town Of Shenzhen, Wiley Online Library on [17/11/2025]. See the Terms and Conditions (https://advanced.onlinelibrary.wiley.com/doi/10.1002/adfm.202504165 by University Town Of Shenzhen, Wiley Online Library on [17/11/2025]. See the Terms and Conditions (https://advanced.onlinelibrary.wiley.com/doi/10.1002/adfm.202504165 by University Town Of Shenzhen, Wiley Online Library on [17/11/2025]. See the Terms and Conditions (https://advanced.onlinelibrary.wiley.com/doi/10.1002/adfm.202504165 by University Town Online Library (https://advanced.onlinelibrary.wiley.com/doi/10.1002/adfm.2

and-conditions) on Wiley Online Library

of use; OA articles are governed by the applicable Creative Commons

www.afm-journal.de

- [7] a) Y. J. Guo, P. F. Wang, Y. B. Niu, X. D. Zhang, Q. Li, X. Yu, M. Fan, W. P. Chen, Y. Yu, X. Liu, Q. Meng, S. Xin, Y. X. Yin, Y. G. Guo, Nat. Commun. 2021, 12, 5267; b) K. J. Park, H. G. Jung, L. Y. Kuo, P. Kaghazchi, C. S. Yoon, Y. K. Sun, Adv. Energy Mater. 2018, 8, 1801202; c) C. Roitzheim, L.-Y. Kuo, Y. J. Sohn, M. Finsterbusch, S. Möller, D. Sebold, H. Valencia, M. Meledina, J. Mayer, U. Breuer, P. Kaghazchi, O. Guillon, D. Fattakhova-Rohlfing, ACS Appl. Energy Mater. 2021, 5, 524; d) W. Yang, W. Xiang, Y.-X. Chen, Z.-G. Wu, W.-B. Hua, L. Qiu, F.-R. He, J. Zhang, B.-H. Zhong, X.-D. Guo, ACS Appl. Mater. Interfaces 2020, 12, 10240.
- [8] a) N. R. Park, M. Zhang, B. Han, W. Li, K. Qian, H. Nguyen, S. Kumakura, Y. S. Meng, Adv. Energy Mater. 2024, 14, 2401968; b) A. Zhou, W. Wang, Q. Liu, Y. Wang, X. Yao, F. Qing, E. Li, T. Yang, L. Zhang, J. Li, J. Power Sources 2017, 362, 131; c) Y. Su, L. Li, L. Chen, L. Wang, Y. Lu, Q. Zhang, L. Bao, F. Wu, ACS Appl. Energy Mater. 2022, 5, 2231.
- [9] a) H. Ren, J. Hu, H. Ji, Y. Huang, W. Zhao, W. Huang, X. Wang, H. Yi, Y. Song, J. Liu, T. Liu, M. Liu, Q. Zhao, F. Pan, Adv. Mater. 2024, 36, 2408875; b) Z. Li, W. Zhao, H. Ren, H. Yi, Y. Du, H. Yu, J. Fang, Y. Song, H. Chen, L. Zhou, S. Li, Q. Zhao, F. Pan, Adv. Energy Mater. 2024, 14, 2402223.
- [10] a) J. Xiao, N. Adelstein, Y. Bi, W. Bian, J. Cabana, C. L. Cobb, Y. Cui, S. J. Dillon, M. M. Doeff, S. M. Islam, K. Leung, M. Li, F. Lin, J. Liu, H. Luo, A. C. Marschilok, Y. S. Meng, Y. Qi, R. Sahore, K. G. Sprenger, R. C. Tenent, M. F. Toney, W. Tong, L. F. Wan, C. Wang, S. E. Weitzner, B. Wu, Y. Xu, Nat. Energy 2024, 9, 1463; b) S. Zhou, J. Yang, C. Zhen, M. D. Gu, M. Shao, Adv. Mater. 2024, 2410199; c) W. Yang, W. Chen, H. Zou, J. Lai, X. Zeng, Y. Zhang, X. Zeng, K. Ding, S. Zhang, L. Ma, Z. Li, Q. Zheng, Angew. Chem., Int. Ed. 2025, 64, 202424353.
- [11] a) W. Wang, L. Wu, Z. Li, K. Huang, Z. Chen, C. Lv, H. Dou, X. Zhang, ChemElectroChem 2021, 8, 2014; b) Y. Zhang, Z. Tang, Y. Mei, Y. Xiao, X. Xiang, D. Luo, J. Deng, Appl. Surf. Sci. 2023, 630, 157488; c) B. You, Z. Wang, Y. Chang, W. Yin, Z. Xu, Y. Zeng, G. Yan, J. Wang, Fundam. Res. 2023, 3, 618.
- [12] a) W. Ding, H. Ren, Z. Li, M. Shang, Y. Song, W. Zhao, L. Chang, T. Pang, S. Xu, H. Yi, L. Zhou, H. Lin, Q. Zhao, F. Pan, Adv. Energy Mater. 2024, 14, 2303926; b) Y. Huang, Y. Dong, Y. Yang, T. Liu, M. Yoon, S. Li, B. Wang, E. Y. Zheng, J. Lee, Y. Sun, Y. Han, J. Ciston, C. Ophus, C. Song, A. Penn, Y. Liao, H. Ji, T. Shi, M. Liao, Z. Cheng, J. Xiang, Y. Peng, L. Ma, X. Xiao, W. H. Kan, H. Chen, W. Yin, L. Guo, W.-R. Liu, et al., Nat. Energy 2024, 9, 1497.
- [13] J. Kikkawa, S. Terada, A. Gunji, T. Nagai, K. Kurashima, K. Kimoto, J. Phys. Chem. C 2015, 119, 15823.

- [14] C. Yogi, D. Takamatsu, K. Yamanaka, H. Arai, Y. Uchimoto, K. Kojima, I. Watanabe, T. Ohta, Z. Ogumi, J. Power Sources 2014, 248, 994.
- [15] W.-H. Hu, Y. Yin, Y. Sun, G.-X. Liu, S.-Y. Yang, Y.-Y. Huang, B. Wang, Rare Met. 2023, 42, 2612.
- [16] a) G. Lelong, L. Cormier, L. Hennet, F. Michel, J.-P. Rueff, J. M. Ablett, G. Monaco, *Inorg. Chem.* **2021**, *60*, 798; b) J. Chen, H. Chen, S. Zhang, A. Dai, T. Li, Y. Mei, L. Ni, X. Gao, W. Deng, L. Yu, G. Zou, H. Hou, M. Dahbi, W. Xu, J. Wen, J. Alami, T. Liu, K. Amine, X. Ji, *Adv. Mater.* **2022**, *34*, 2204845.
- [17] a) F. Li, Z. Liu, C. Liao, X. Xu, M. Zhu, J. Liu, ACS Energy Lett. 2023, 8, 4903; b) W. Zheng, G. Liang, H. Guo, J. Li, J. Zou, J. A. Yuwono, H. Shu, S. Zhang, V. K. Peterson, B. Johannessen, L. Thomsen, W. Hu, Z. Guo, Energy Environ. Sci. 2024, 17, 4147; c) S. Gao, B. Shi, J. Liu, L. Wang, C. Zhou, C. Guo, J. Zhang, W. Li, ACS Sustainable Chem. Eng. 2021, 9, 5322.
- [18] Y. Lu, C.-Z. Zhao, J.-Q. Huang, Q. Zhang, Joule 2022, 6, 1172.
- [19] B. L. D. Rinkel, D. S. Hall, I. Temprano, C. P. Grey, JACS 2020, 142, 15058.
- [20] Y. Li, Y. Li, A. Pei, K. Yan, Y. Sun, C.-L. Wu, L.-M. Joubert, R. Chin, A. L. Koh, Y. Yu, J. Perrino, B. Butz, S. Chu, Y. Cui, Science 2017, 358, 506.
- [21] a) N. R. Park, M. Zhang, B. Han, W. Li, K. Qian, H. Nguyen, S. Kumakura, Y. S. Meng, Adv. Energy Mater. 2024, 14, 2401968; b) N. R. Park, Y. Li, W. Yao, M. Zhang, B. Han, C. Mejia, B. Sayahpour, R. Shimizu, B. Bhamwala, B. Dang, S. Kumakura, W. Li, Y. S. Meng, Adv. Funct. Mater. 2024, 34, 2312091; c) P. Bai, X. Ji, J. Zhang, W. Zhang, S. Hou, H. Su, M. Li, T. Deng, L. Cao, S. Liu, X. He, Y. Xu, C. Wang, Angew. Chem., Int. Ed. 2022, 61, 202202731.
- [22] H. Yu, J. Cheng, H. Zhu, L. Chen, C. Lian, Y. Hu, H. Liu, H. Jiang, C. Li, Adv. Mater. 2025, 37, 2412360.
- [23] a) B. Zhang, G. Shi, Z. Yang, F. Zhang, S. Pan, Angew. Chem., Int. Ed. 2017, 56, 3916; b) G. Cakmak, J. Nuss, M. Jansen, Z. Anorg. Allg. Chem. 2009, 635, 631; c) A. Tudi, H. Zeng, C. Xie, E. Tikhonov, S. Han, S. Pan, Z. Yang, Chem. Mater. 2022, 34, 3133; d) T. Pilz, M. Jansen, Z. Anorg. Allg. Chem. 2011, 637, 2148.
- [24] a) Z. Zhu, S. Xu, Z. Wang, X. Yan, G. Xu, Y. Huang, Y. Wu, Y. Zhang, J. Li, *Energy Environ. Sci.* 2024, 17, 6102; b) M. Zhang, W. Huang, J. Tang, Z. Liu, C. Sheng, X. Sun, H. Zhong, S. Xu, W. Ning, X. Xiao, T. Liu, S. Guo, H. Zhou, *JACS* 2025, 147, 1563.
- [25] Z. Wu, G. Zeng, J. Yin, C.-L. Chiang, Q. Zhang, B. Zhang, J. Chen, Y. Yan, Y. Tang, H. Zhang, S. Zhou, Q. Wang, X. Kuai, Y.-G. Lin, L. Gu, Y. Qiao, S.-G. Sun, ACS Energy Lett. 2023, 8, 4806.